Edinburgh Research Explorer

Structural transitions in a ring stain created at the contact line of evaporating nanosuspension sessile drops

Structural transitions in a ring stain created at the contact line of evaporating nanosuspension sessile drops

Alexandros Askounis,[1] Khellil Sefiane,[1] Vasileios Koutsos,[1,*] and Martin E. R. Shanahan[2,3,4]

[1]*Institute for Materials and Processes, School of Engineering, The University of Edinburgh, King's Buildings, Mayfield Road, Edinburgh, EH9 3JL, United Kingdom*
[2]*University of Bordeaux, I2M, UMR 5295, F-33400 Talence, France*
[3]*CNRS, I2M, UMR 5295, F-33400 Talence, France*
[4]*Arts et Metiers ParisTech, I2M, UMR 5295, F-33400 Talence, France*

Monodisperse nanosuspension droplets, placed on a flat surface, evaporated following the stick-slip motion of the three-phase contact line. Unexpectedly, a disordered region formed at the exterior edge of a closely packed nanocolloidal crystalline structure during the "stick" period. In order to assess the role of particle velocity on particle structuring, we did experiments in a reduced pressure environment which allowed the enhancement of particle velocity. These experiments revealed the promotion of hexagonal packing at the very edge of the crystallite with increasing velocity. Quantification of particle velocity and comparison with measured deposit shape for each case allowed us to provide a tentative description of the underlying mechanisms that govern particle deposition of nanoparticles at the triple line of an evaporating droplet. Behavior is governed by an interplay between the fluid, and hence particle, flow velocity (main ordering parameter) and wedge constraints, and consequently disjoining pressure (main disordering parameter). Furthermore, the formation of a second disordered particle region at the interior edge of the deposit (towards bulk fluid) was found and attributed to the rapid motion of the triple line during the "slip" regime. Additionally, the magnitude of the pinning forces acting on the triple line of the same drops was calculated. These findings provide further insight into the mechanisms of the phenomenon and could facilitate its exploitation in various nanotechnological applications.

I. INTRODUCTION

The evaporation of sessile droplets containing particles has attracted considerable scientific interest over the past few years. It was found that when such a droplet evaporates, it leaves behind a ring stain which is now well known as the "coffee stain" effect [1–3]. When nanoparticles were introduced, the droplet evaporated following what is described as "stick-slip" behavior [4]. This behavior was shown experimentally using TiO_2 nanosuspensions both at the macroscale [5,6] and the nanoscale [7]. In another work, nanoparticle terrace formation (indicative of particle crystals) at the receding edge of an evaporating droplet was predicted by (theoretically) implementing particle interactions as structural disjoining pressure effects [8].

Particle structuring within deposits left behind after evaporation has been reported for suspensions of various geometries. Nanorods assembled into superlattices with clear particle arrays [9] and ribbonlike structures [10]. Spheres led to hexagonal structures at the contact line of evaporating suspensions in a wedge geometry [11–16]. Binary suspensions also exhibited hexagonal packing tendency [17] and various other structuring types [18,19]. Elsewhere [20], an order to disorder transition was attributed to microspheres arriving at the contact line of an evaporating droplet at a slow but increasing speed, allowing free particle motion and hence ordering. Upon reaching a critical particle velocity, particles arrive too fast at the contact line, thus forming random disordered regions. Based on their

observations these authors [20] suggested that a coffee stain of a nanosuspension will consist of perfect crystals.

Particle structuring effects have also been related to other experimental parameters, i.e., geometry and controlled evaporation. In forced dewetting (substrate retracting from a nanofluid pool), striped deposits with some degree of ordering occurred due to a combination of capillary forces and fluid evaporation [21–25]. When the colloidal fluid was confined in well-defined wedges (glass slides in a triangular configuration), particle crystallites with square and triangular ordered regions formed. These formations were attributed to particles attempting to maintain the highest possible volume fraction within the wedge confinement as the height increased and each new layer formed [26,27]. Similar ordered regions were reported in other cases of confined geometries [28,29] or when capillary forces were used to form stripe patterns [30,31] and for flat capillaries [32,33].

As discussed above, particle crystallization is expected in the case of evaporating sessile droplets containing very small particles (<100 nm) [20]. However, in this contribution, we report on disordered regions forming at both edges of a close-packed particle crystallite. These amorphous structures formed at the contact line of a monodisperse, colloidal nanosuspension sessile drop following evaporation accompanied by stick-slip triple line (TL) motion. This is of major importance since these structures were unexpected for nanoparticles. Therefore, we provide a tentative plausible explanation. Further understanding and control of the underlying mechanisms of this phenomenon could provide a quick and inexpensive way of bottom-up assembling of desired patterns on surfaces, tailored to individual needs of nanotechnological applications.

---

*Author to whom correspondence should be addressed: vasileios.koutsos@ed.ac.uk

II. EXPERIMENTAL METHODOLOGY

Monodisperse, spherical, nonporous SiO_2 particles were chosen in this study in order to avoid polydispersity effects. Polydispersity was reported to limit crystallization [7,14]. The particles were obtained in concentrated solution from Klebosol, AZ Electronic Materials France SAS, Trosly-Breuil, France. Particle diameter is 80 nm and the ζ potential is about -30 mV at pH 9 (as specified by the manufacturer). Drops of 0.125 wt % solution (3 μl) were gently deposited on silicon substrates (covered with a native oxide layer), using the automated dosage system of a Krüss DSA100 (Krüss GmbH, Hamburg, Germany) drop shape analyzer (DSA). Experiments were carried out inside a low pressure chamber (lower limit of 40 mbar) which allows precise control of the environment around the drop. Additionally, the high-speed camera of the DSA recorded the evolution of the drop (contact radius, contact angle, volume) through windows on both sides of the chamber. Prior to use, the suspension was stabilized by sonication for 30 min. Substrates were cleaned in an ultrasonic bath of isopropanol for 15 min and dried under a stream of compressed air. The above procedure was repeated several times in order to establish reproducibility and each sample was imaged at several different areas of interest and of different sizes. Here, we present representative images of the deposits acquired by optical microscopy and atomic force microscopy (AFM).

AFM imaging was conducted using a Bruker MultiMode Nanoscope IIIa AFM (Bruker AXS, Santa Barbara, CA), equipped with a J scanner (x–y scan range $\sim$140 μm). The samples were imaged in tapping mode (tip in intermediate contact with the surface). RTESPA Bruker cantilevers with nominal spring constant of 40 N/m and resonance frequency of 300 kHz were used to image the samples. Nominal tip radius was 8 nm, as specified by the manufacturer. All scans were performed in air at room temperature. Acquired images were postprocessed by simple flattening and analysis including height profiles and fast Fourier transformations (FFTs) using the software SCANNING PROBE IMAGE PROCESSOR (SPIP, Image Metrology, Hørsholm, Denmark).

III. RESULTS AND DISCUSSION

Free evaporation of an aqueous suspension droplet containing 0.125 wt % SiO_2 nanoparticles followed the "stick-slip" regime and the resulting pattern is presented in Fig. 1(a). In
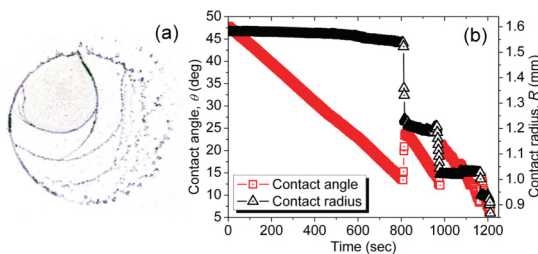

FIG. 1. (Color online) (a) Optical micrograph of the coffee stain left behind after the evaporation of a freely evaporating aqueous suspension drop containing 0.125 wt % SiO_2 nanoparticles. (b) Evolution of contact angle (squares) and contact radius (triangles) for same drop.

Fig. 1(b) the evolution of both the contact radius and angle of the droplet is presented. Basically, the TL remains anchored for a period during which evaporation leads to particle deposition (stick), followed by rapid TL motion (slip) to a subsequent state of quasiequilibrium. In the evolution graph [Fig. 1(b)] only two "jumps" of the TL are clearly identifiable mainly due to the orientation of the camera while recording the movement of the TL. The average evaporation rate of the droplet was calculated to be $\sim$2.5 nl/s, in accordance with the literature [34].

Let us consider, here, the evolution of the excess free energy, δG, of the drop during evaporation, over the equilibrium value, $G(\theta_0)$, assuming that the contact radius, R, remains constant. Neglecting gravity effects since the drop is small, at a given instant, when contact angle is θ and free energy is $G(\theta)$, we have [4]

$$\delta G = G(\theta) - G(\theta_0) = \gamma \pi \left\{ R^2 \left[\frac{2}{(1 + \cos\theta)} - \cos\theta_0 \right] \right.$$
$$\left. - R_0^2 \left[\frac{2}{(1 + \cos\theta_0)} - \cos\theta_0 \right] \right\}. \quad (1)$$

The term R_0 corresponds to the radius of a drop of equal volume to the actual drop, but at equilibrium ($R \geqslant R_0$). Clearly, R_0 decreases as evaporation continues, although θ_0 does not, since volume, V, decreases. At a given instant, for given V, we have

$$V = \frac{\pi R^3}{3 \sin^3\theta} (1 - \cos\theta)^2 (2 + \cos\theta)$$
$$= \frac{\pi R_0^3}{3 \sin^3\theta_0} (1 - \cos\theta_0)^2 (2 + \cos\theta_0). \quad (2)$$

Isolating R_0^2 in Eq. (2) and inserting it in Eq. (1) we obtain

$$\delta G = \frac{\gamma \pi R^2}{(1 + \cos\theta)} \left[2 - \cos\theta_0 (1 + \cos\theta) - (1 - \cos\theta)^{1/3} \right.$$
$$\left. \times (2 + \cos\theta)^{2/3} (2 + \cos\theta_0)^{1/3} (1 - \cos\theta_0)^{2/3} \right]. \quad (3)$$

We can thus calculate the excess free energy, per unit length of TL, $\delta\overline{G}$, at any instant during evaporation from $\delta\overline{G} = \delta G / (2\pi R)$. With knowledge of R during a given phase of evaporation, the value of θ at the moment in question, and the equilibrium angle, θ_0, the evolution of $\delta\overline{G}$ can be followed. When a jump of R to a smaller value occurs, it may be considered that $\delta\overline{G}$ has attained the value of the hysteresis jump barrier.

Liquid surface tension, γ, was measured using the pendant drop technique to be that of pure water, $\sim$0.073 N/m. The evolution of $\delta\overline{G}$ is plotted in Fig. 2.

In Fig. 2, $\delta\overline{G}$ increases, initially, due to the pinned TL and the decreasing contact angle. During this stage, the deposit (ring) builds up. At $\sim$800 s, $\delta\overline{G}$ reaches a maximum value of $\sim$1.7 $\times$ 10^{-5} N, which is an order of magnitude larger than what has been reported previously for a similar system [6]. This could be attributed to the more refined calculation of $\delta\overline{G}$, here. At this point, $\delta\overline{G}$ reaches a threshold value (hysteresis jump barrier). This leads to a TL jump to a new smaller R with higher θ (as seen in Fig. 1), leading to a cutoff in particle accumulation and/or deposition. Essentially, at this point the system "freezes," allowing no local order to be developed. Given the evaporation behavior of the drop
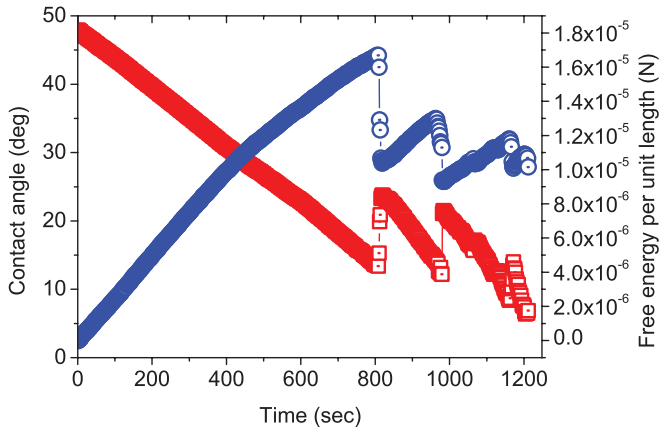
FIG. 2. (Color online) Evolution of contact angle (squares) and free energy per unit length of TL, $\delta\overline{G}$ (circles) for an aqueous suspension drop containing 0.125 wt % SiO_2 nanoparticles evaporating under 1000 mbar pressure.

FIG. 3. (Color online) (a) Optical micrograph depicting part of the ring stain. (b) 3.32×3.32 μm^2 topography image [dotted box in (a)] with three different areas of interest highlighted, z scale ranges between 0 and 1.25 μm. (i)–(iii) FFT analysis of the areas highlighted in the topography image (b); dotted lines are a guide to particle packing.

(i.e., stick-slip), the first jump requires slightly higher energy, 1.7×10^{-5} N compared to $\sim 1.2 \times 10^{-5}$ N for the rest of the jumps, indicative of the effect of local particle accumulation on the pinning forces. In addition, the first jump corresponds to the case where the solid outside the drop has not "seen" the liquid. For subsequent jumps, the solid outside has already been wet by the liquid and it is therefore probable that an adsorbed liquid layer decreases the energy barrier to some extent. This cycle continues until full evaporation of the liquid and the rest of the rings are formed. Some irregularities (especially towards the end of evaporation) in both curves in Fig. 2 are probably due to uncertainties in measuring $\delta\theta$, since the drop periphery is not perfectly circular.

In order to examine the resulting pattern and probe possible particle structuring, we used optical microscopy and AFM. Optical microscopy of part of the ring stain [Fig. 3(a)] revealed a clear striped region, visible as an optical interference pattern, at the side towards the exterior of the drop (left side of stain). This region indicates a gradual increase in deposit height. Some cracks on the deposit are also visible in the image, attributable possibly to the uncontrolled character of the evaporation process. However, they are outside the scope of this work and will be addressed in the future.

Particle self-assembly, revealed by AFM, at the edge of the ring stain [a representative area highlighted in Fig. 3(a), corresponding to the receding edge] is presented in Fig. 3(b). Systematic analysis of the deposits unveiled the formation of a narrow disordered region at the very edge of the deposit (corresponding to the receding droplet front). Moreover, AFM revealed transitions between successive narrow-, square-, and hexagonal-packed regions within the deposit. Typical examples of each of these regions are highlighted with white boxes in Fig. 3(b) corresponding to each of the three areas, respectively. These regions were analyzed by FFT [Figs. 3(i)–3(iii)] in order to determine particle structuring. Near the contact line [region (i)], particles assembled in random positions forming a narrow, disordered region [verified by smeared FFT (i)]. This formation could be attributed to a combination of (a) small particle size, thus allowing particles
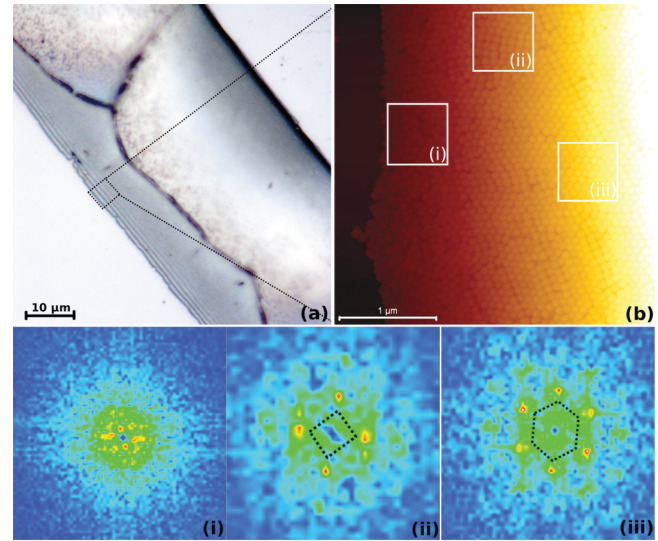
to travel very close to the actual contact line of the drop where the wedge area between the liquid-vapor interface and the solid substrate lead to stronger disjoining pressures, (b) higher evaporation at the drop periphery, and (c) strong laminar solute flux towards the TL, the last two being directly linked. A detailed description and analysis of this disordering mechanism will be presented later in this paper. As solute continues to be transferred from the center of the drop towards the periphery, particles far from the contact line and within the deposit are allowed more freedom to move [35] due to weaker geometrical constraints. Thus, two different types of close-packed formations are formed. These two types consist of a sequence of narrow, square-packed [presented in region (ii) of Fig. 3] and hexagonal areas [highlighted as region (iii) in Fig. 3] and are probably correlated to deposit height as indicated in Fig. 3(b).

An order to disorder transition for evaporating colloidal drops has been reported recently, although with two distinct differences: particle size and evaporation mechanism [20]. In our case, the droplet evaporates following stick-slip behavior while in the previous case, the contact line of the droplet remained constantly pinned, to be discussed below. Particle diameters, d, in our study are at least 10 times smaller than those in the earlier paper [20], D ($d \sim 80$ nm compared to $D \sim 0.5$–2 μm). The particles in our case can get closer to the actual contact line of the evaporating drop (see Fig. 4). The wedge shape constraints and structural disjoining pressure due to the *nano*-particles are much stronger compared to those affecting *micro*-spheres. Due to height restrictions, particles are necessarily smaller than the droplet height, h_w, at the very edge of the contact line. The approach distance, ℓ, is simply given by $d \cot\theta$ (or $L = D \cot\theta$ for the microspheres of Ref. [20]). For small contact angle, θ, this difference in distance from the TL to the first particle will be considerable
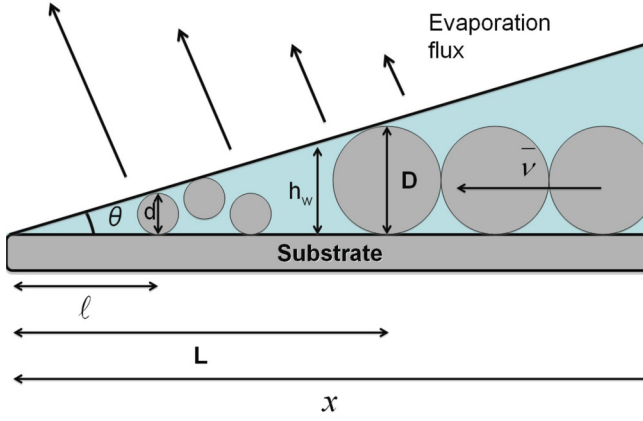
FIG. 4. (Color online) Schematic representation of the first particle distance (ℓ, L) dependence on particle diameter (d, D) at the receding front.

for the two cases and can be calculated as follows:

$$(L - \ell) = (D - d) \cot \theta \approx D \cot \theta. \tag{4}$$

From the above simple argument, we estimate for a contact angle of $\sim 50°$ that micrometric particles [20] may approach the TL only to within ~ 0.4 μm or more (varying with particle diameter). However, nanoparticles may get within ~ 65 nm, the domain where stronger evaporative effects may be felt, leading to faster and less ordered particle precipitation. At such small distances from the TL, with nanoparticles, "conventional" disjoining pressure effects may also be felt where the liquid thickness is comparable to particle diameter. As a consequence, both conventional and structural disjoining pressures are relevant, whereas for micrometric particles, only the latter applies. The above argument is schematically presented in Fig. 4.

The above discussion is indicative of the interplay between particle velocity and disjoining pressure, which could be responsible for the formation of the observed narrow disordered region. In what follows, we attempt to assess this possibility by combining theoretical and experimental arguments. To achieve this, we increased the radial fluid velocity by lowering the ambient pressure to 750 and 500 mbar. Evaporation flux is known to be higher at the periphery of a pinned droplet, where outward fluid flow is induced in order to replenish that lost by evaporation [1,2,36]. Lowering the pressure increased the average evaporation rate to ~ 3.8 and 7.5 nl/s for 750- and 500-mbar cases, respectively. Additionally, two different types of TL behavior during evaporation were observed: stick-slip motion and constant pinning of the TL. Evaporation flux is dependent on vapor diffusivity, which in turn is connected to pressure via the formula $D_{ua} \approx D_{ref} P_{ref} / P$ (where $D_{ref} = 2.4 \times 10^{-5}$ m²/s is the value of D_{ua} at the reference pressure $P_{ref} = 1000$ mbar) [37]. This simple formula was introduced into the height-averaged radial velocity, $\bar{v}$, an equation proposed in Refs. [20,38], leading to

$$\bar{v}(r, t, P) = \frac{4 \Delta c R(t)}{\pi \rho r \theta(t)} \left[\frac{1}{\sqrt{R^2(t) - r}} - \frac{R^2(t) - r^2}{R^3(t)} \right] \frac{D_{ref} P_{ref}}{P}, \tag{5}$$
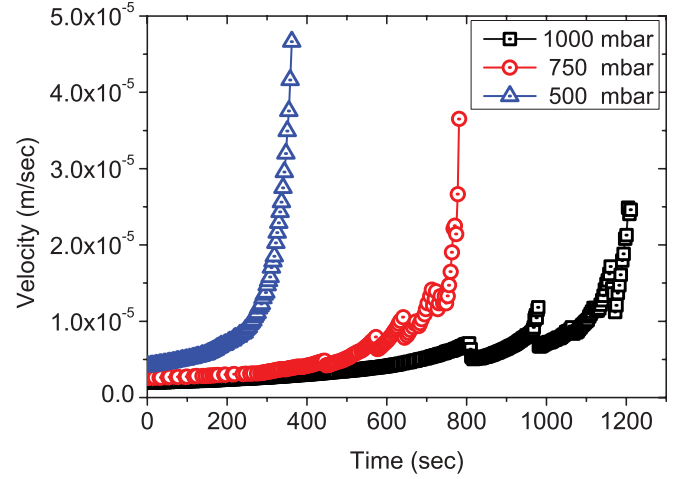

FIG. 5. (Color online) Velocity evolution of particles arriving at the edge ($r = 0.99R$) of the drop during evaporation under 1000, 750, and 500 mbar pressure.

where θ and R are contact angle and contact radius, and r is radial distance. Vapor concentration difference between drop surface and the surroundings, $\Delta c = 1.9 \times 10^{-2}$ kg/m³ and liquid density, $\rho = 1000$ kg/m³.

Since we focus our attention on the wedge area very near the TL, we solved Eq. (5) for $r = 0.99R$ for each of the three different pressures. Plotting our results in Fig. 5 shows that particle velocity increases as pressure decreases. Particle velocity was found to increase from a maximum of about 2.5×10^{-5} m/s at ambient conditions (1000 mbar) to 3.6×10^{-5} m/s when pressure was lowered to 750 mbar and to 4.7×10^{-5} m/s when pressure was further reduced to 500 mbar. Some peaks in the graphs of the two stick-slip cases (1000 and 750 mbar) can be identified. These peaks correspond to jumps of the TL and are a result of the dependency of Eq. (5) on θ and R. The effect of this increasing velocity on particle structuring will be established next. These results are in accordance with the velocity calculated in the case of a constantly pinned drop [20] but have not been reported before for stick-slip evaporation.

AFM imaging unveiled that increasing particle velocity promotes crystallinity. This is presented in Fig. 6, which shows the topography image of the deposits for 1000, 750, and 500 mbar, respectively, from (a) to (c). Individual particles in these images are difficult to distinguish due to the size of each image (5×5 μm²). For this reason, we provide as an inset (bottom) the magnification of a random area of interest near the deposit edges [similar to the area presented in Fig. 3(i). In addition, FFT analyses of the same areas is presented in the top inset in every image. A second interesting observation in these images is the fact that an increased evaporation rate results in a decrease in the deposit slope, which in turn leads to an increase in the wedge constraints. This is depicted in Fig. 6(d), where the average colored height profiles were acquired from several height profiles such as the ones corresponding to colored lines in Figs. 6(a)–6(c). The limitation of the available space is further highlighted in the inset of Fig. 6(d), which is a magnification of the first 0.5 microns of each of the three height profiles and shows the first pinning site (i.e., where the first particles arrive in each case to pin the TL). It is within
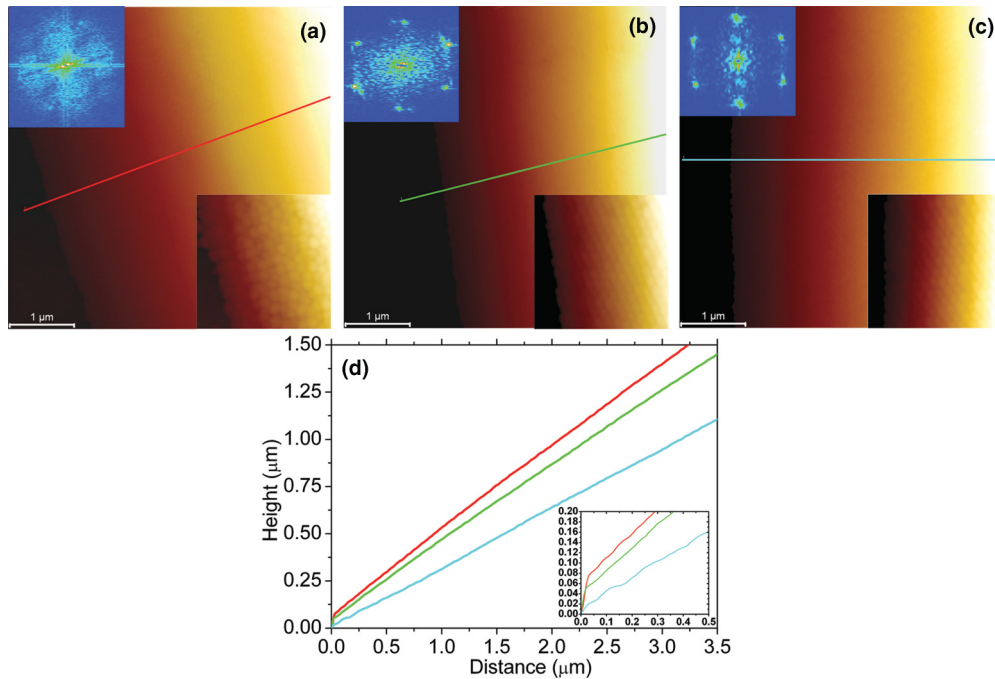
FIG. 6. (Color online) 5.0×5.0 μm^2 topography images corresponding to deposits produced after the evaporation under environmental pressures of 1000, 750, and 500 mbar, respectively from (a)–(c). Insets (bottom) present magnified areas of random positions of interest near deposit edges and insets (top) correspond to FFT analyses of same areas. All insets highlight the promotion of crystallinity at the edge with increasing velocity. (d) Average height profiles acquired from several height profiles such as the ones corresponding to colored lines in (a)–(c), respectively.

this narrow region that the disorganized structure was found in the 1000-mbar case and therefore the reason why we focus our attention there.

Combining these two results together (velocity effect and disjoining pressure), we can speculate that particle velocity is the main ordering parameter and disjoining pressure is acting as a disordering barrier. This argument is better exhibited in Fig. 7, where the deposit height is plotted against the calculated
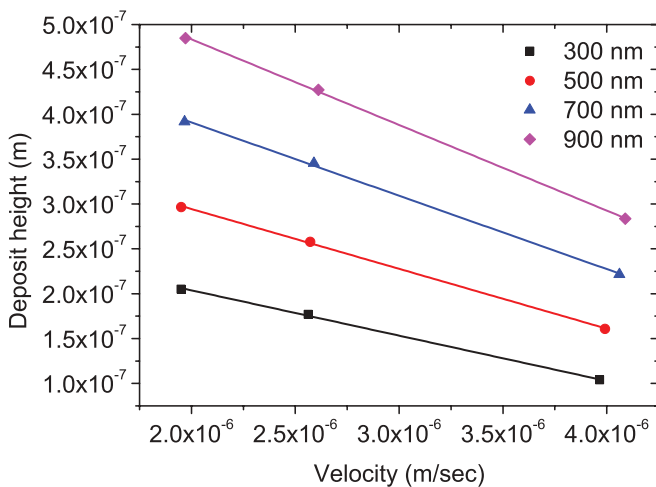

FIG. 7. (Color online) Deposit height at a distance periphery of drop of 300, 500, 700, and 900 nm [corresponding to black (square), red (circle), blue (triangle), and pink (diamond) lines, respectively] vs calculated particle velocity speed at same distance for 1000 mbar (points on the left), 750 mbar (points in center), and 500 mbar (points on the right).

particle velocity [using Eq. (5)] at certain distances away from the periphery of the drop (namely 300, 500, 700, and 900 nm corresponding to black, red, blue, and pink lines, respectively) and within the deposit for all three cases. The velocities presented here are about an order of magnitude smaller than the maximum velocities presented in Fig. 5. This difference is expected due to the fact that particle velocity was found to increase rapidly before each slip of the TL for the stick-slip cases, or toward the end of the evaporation cycle in pinned drops, as shown in Fig. 5. This behavior could be attributed to mass conservation and is in accordance with the literature [20]. We could presume at this point that decreasing deposit height (Fig. 7) should lead to increasing disjoining pressures, hindering particle motion. However, the effect of the disjoining pressures acting as a disordering barrier is probably overcome by the increasing particle velocity (Fig. 7, middle and right-side points corresponding to 750 and 500 mbar, respectively), giving rise to the observed crystalline structures [Figs. 6(b), 6(c)]. The relation between deposit heights and velocities was found to be linear, of the form $y = a + bx$ with a slope of $-0.09 < b < -0.04$.

The simple argument presented here provides a tentative, plausible explanation of the formation of a disordered region at the exterior edge of a particulate deposit left behind after the evaporation of a nanosuspension drop.

The rest of the deposit near the TL [Fig. 3(b)] consists of sequential hexagonal and narrow, square-packed regions, which are in agreement with what has been previously reported for experimental setups different from ours (i.e., controlled evaporation, larger sized particles, different geometry) [30,39–41]. The succession of these two types of structuring was attributed to the most efficient particle packing within the limited space
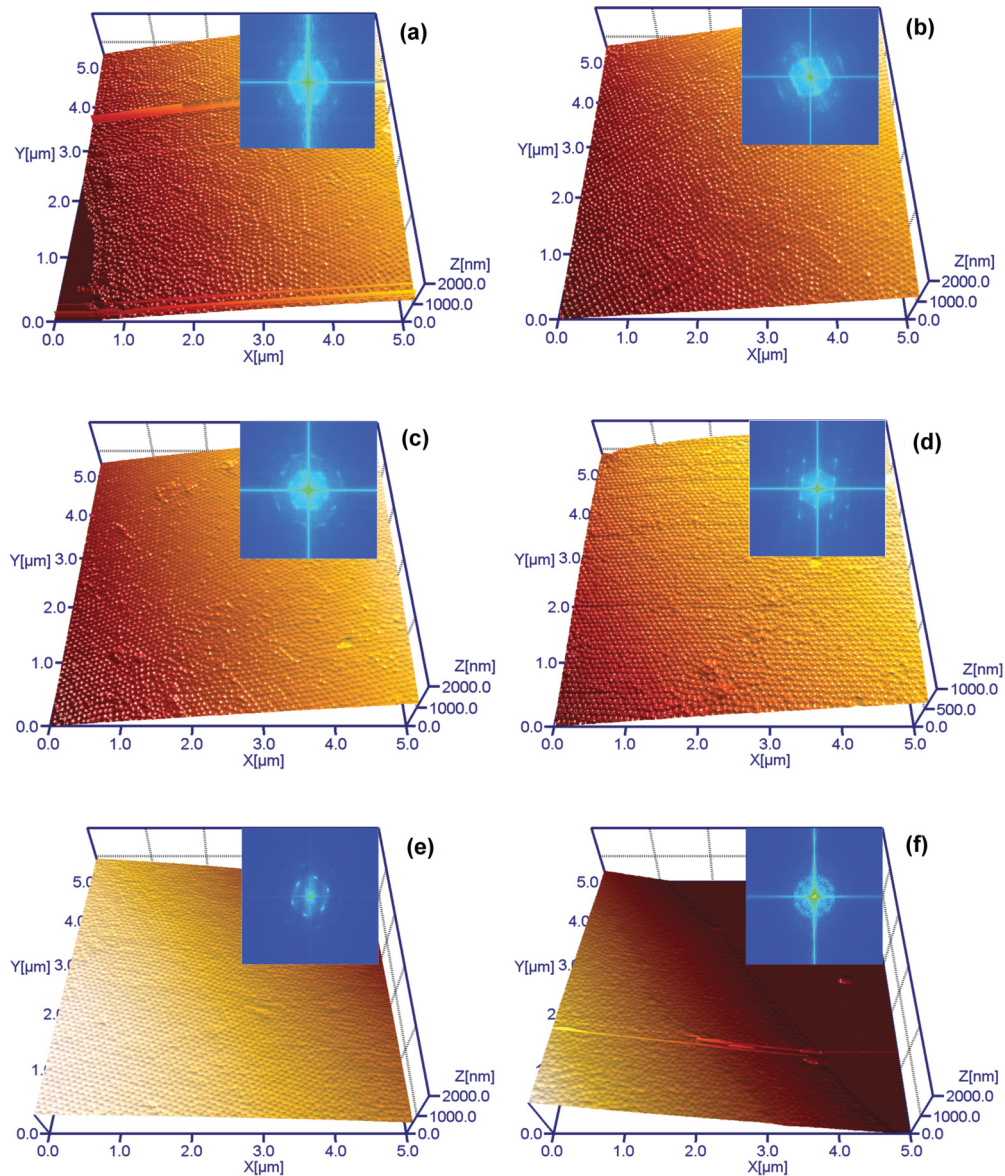
FIG. 8. (Color online) (a)–(f) Characteristic, consecutive $5 \times 5 \ \mu m^2$ three-dimensional representations of areas across the ring stain width of the 1000-mbar case. z scale in each image is zeroed to the top of the previous image for better illustration. Insets correspond to FFT analysis of each image.

as thickness increases. This crystallization could also be correlated with particle terraces (terracing requires particles to attain a degree of ordering which leads to crystals), which have been previously predicted for evaporating colloidal drops where particle interactions were implemented as structural disjoining pressure effects [8]. However, in our case, only short terraces were observed. We believe that our observation of terracing for a free evaporating sessile drop, containing particles of this size range (~80 nm), is significant.

The effect of radial position on particle structuring was also determined. In previous work [7], we concluded that the radial position had no noticeable effect on stain geometry for a system whose main difference was particle polydispersity. In this case, we imaged several samples at different areas of different rings. All areas exhibited similar structuring, therefore we concluded that radial position had negligible or

no effect on particle structuring, at least for the system in question.

The dependency of particle ordering on deposit height and the overall ordering tendency were additionally established. To do so, we scanned across the width of the ring stain left behind the freely evaporating drop (1000 mbar) using AFM. In Fig. 8 we present six sequential images of the areas scanned. Imaging was done and results are presented in such a way as to allow observation of both deposit height and crystal structure. The other two cases (750 and 500 mbar) were also scanned across the width of the ring stain; however, they are not presented here since they exhibited similar packing behavior and deposit shape.

In Figs. 8(a) and 8(f), an order to disorder transition can be observed to occur at both edges of the deposit. Figure 8(a) shows a representative area near the contact line where
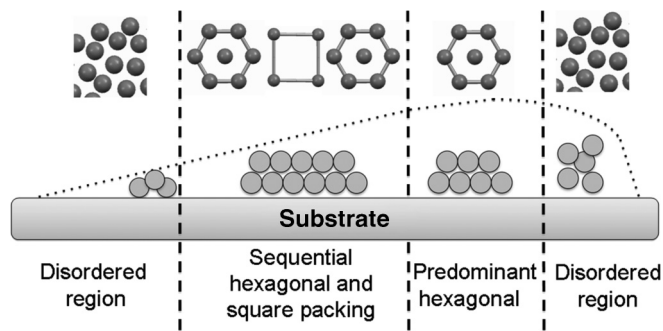
FIG. 9. Schematic representation of different ordering types in different regions within a typical ring stain formed during evaporation under 1000 mbar.

particles arranged themselves firstly into a narrow disordered region which was followed by close-packed structures for the reasons discussed above. Figure 8(f) is a typical area at the drop edge towards the interior of the drop. Although a similar order to disorder transition at the ring edge towards the interior of the drop has been reported elsewhere, it was attributed to a different phenomenon, that of increasing particle velocity (or "rush hour" effect) [20]. The deposition rate of particles at the contact line (due to the flow described by Deegan *et al.* [2]) is probably so fast, in that case, that free particle motion is hindered and thus leads to the disordered areas reported. The case described in Ref. [20] corresponds to permanent TL pinning, where the whole depositing process occurs in the same annular region. In our case, stick-slip behavior occurs [4], which, as described above, leads to an abrupt cutoff of particle deposition due to TL jumping [very rapid motion as seen in Figs. 1(b) and 2] to a more favorable position. Essentially, particles will freeze forcing the formation of the observed disordered region at the interior edge of the drop.

The rest of the ring stain was found to consist of sequential hexagonal and narrow square-packed regions, as presented in Figs. 8(b)–8(e). In more detail, Figs. 8(b) and 8(c) show that as deposit height increased, particle ordering was promoted leading to mainly hexagonal structures but also to some square-packed regions (FFT insets, where the hexagonal cell becomes gradually clearer). At the very peak of the deposit [Fig. 8(d)], almost perfect hexagonal packing was achieved. This could be attributed to a lack of wedge constraints, which arises from the extra volume and results in more space and less disjoining pressure effects, thus accommodating particle free motion to the most favorable positions. Indeed hexagonal packing leads to a higher particle density and is thermodynamically more favorable [23]. In Fig. 8(e), the hexagonal structuring was found to be interrupted by narrow,

square-packed areas (FFT became more blurry), presumably due to the deposit height decreasing sharply and therefore making wedge constraints more effective [7]. Hence, we can deduce from these images that *particle ordering is dependent on deposit height*. In addition, it should be noted how steep the slope of this side of the ring is, again due to the quick jump of the contact line. Particle ordering in a sequence of hexagonal and square-packed areas was reported to have occurred in other cases, mainly due to capillary forces in a cylindrical geometry [30] or when a tilted substrate was withdrawn from a nanofluid pool [23,39]. A schematic summarizing the main structured regions of the ring stain is presented in Fig. 9.

IV. CONCLUSIONS

The free evaporation of sessile drops of monodisperse nanofluids has been found to lead to nanoparticle crystal formation. Evaporation was observed to follow both pinned triple line (TL) behavior and stick-slip TL jumping, depending on conditions, notably ambient pressure. We report on the unexpected formation of a disordered region at the exterior of a ring stain deposit. Increasing flow velocity by reducing environmental pressure was found to promote crystallinity. Quantification of particle velocity and comparison with experimental results allowed us to attribute the formation of this disordered region to the interplay between particle velocity (main ordering parameter) and disjoining pressures (main disordering parameter). A similar disordered region formed at the interior edge (closer to bulk fluid) as a result of the rapid TL motion during the slip phase which essentially freezes the particles in place.

The rest of the deposit consisted of mainly hexagonal-packed structures. Occasionally, square-packed structures were also found to interrupt the hexagonal formations as each particle layer was formed. This sequencing was attributed to particles trying to achieve the highest possible volume fraction within the limited wedge space. Deposit height was also found to promote crystallinity.

An attempt to quantify the pinning barriers acting on the TL was made by calculating the evolution of the excess free energy of the system, which just before each jump exhibited a peak and should be equivalent to the pinning forces.

[1] R. D. Deegan, O. Bakajin, T. F. Dupont, G. Huber, S. R. Nagel, and T. A. Witten, Nature **389**, 827 (1997).

[2] R. D. Deegan, O. Bakajin, T. F. Dupont, G. Huber, S. R. Nagel, and T. A. Witten, Phys. Rev. E **62**, 756 (2000).

[3] R. D. Deegan, Phys. Rev. E **61**, 475 (2000).

[4] M. E. R. Shanahan, Langmuir **11**, 1041 (1995).

[5] J. R. Moffat, K. Sefiane, and M. E. R. Shanahan, J. Phys. Chem. B **113**, 8860 (2009).

[6] D. Orejon, K. Sefiane, and M. E. R. Shanahan, Langmuir **27**, 12834 (2011).

[7] A. Askounis, D. Orejon, V. Koutsos, K. Sefiane, and M. E. R. Shanahan, Soft Matter **7**, 4152 (2011).

[8] R. V. Craster, O. K. Matar, and K. Sefiane, Langmuir **25**, 3601 (2009).

[9] Y. Xie, S. M. Guo, Y. L. Ji, C. F. Guo, X. F. Liu, Z. Y. Chen, X. C. Wu, and Q. Liu, Langmuir **27**, 11394 (2011).

[10] C. Nobile, L. Carbone, A. Fiore, R. Cingolani, L. Manna, and R. Krahne, J. Phys.: Condens. Matter **21**, 264013 (2009).

[11] A. D. Nikolov, and D. T. Wasan, Ind. Eng. Chem. Res. **48**, 2320 (2009).

[12] L. Shmuylovich, A. Q. Shen, and H. A. Stone, Langmuir **18**, 3441 (2002).

[13] C. Monteux and F. Lequeux, Langmuir **27**, 2917 (2011).

[14] M. Evers, H.-J. Schöpe, T. Palberg, N. Dingenouts, and M. Ballauff, J. Non-Cryst. Solids **307-310**, 579 (2002).

[15] M. Evers, T. Palberg, N. Dingenouts, M. Ballauff, H. Richter, and T. Schimmel, in *Trends in Colloid and Interface Science XIV*, edited by V. Buckin, Progress in Colloid and Polymer Science Vol. 115 (Springer, Berlin/Heidelberg, 2000).

[16] N. D. Denkov, H. Yoshimura, K. Nagayama, and T. Kouyama, Phys. Rev. Lett. **76**, 2354 (1996).

[17] K. P. Velikov, C. G. Christova, R. P. A. Dullens, and A. van Blaaderen, Science **296**, 106 (2002).

[18] E. V. Shevchenko, D. V. Talapin, N. A. Kotov, S. O'Brien, and C. B. Murray, Nature **439**, 55 (2006).

[19] D. V. Talapin, E. V. Shevchenko, M. I. Bodnarchuk, X. Ye, J. Chen, and C. B. Murray, Nature **461**, 964 (2009).

[20] A. G. Marín, H. Gelderblom, D. Lohse, and J. H. Snoeijer, Phys. Rev. Lett. **107**, 085502 (2011).

[21] S. Watanabe, K. Inukai, S. Mizuta, and M. T. Miyahara, Langmuir **25**, 7287 (2009).

[22] J. A. Lee, K. Reibel, M. A. Snyder, L. E. Scriven, and M. Tsapatsis, Chem. Phys. Chem. **10**, 2116 (2009).

[23] H. Cong and W. X. Cao, Langmuir **19**, 8177 (2003).

[24] A. S. Dimitrov and K. Nagayama, Langmuir **12**, 1303 (1996).

[25] J. Hilhorst, M. M. van Schooneveld, J. Wang, E. de Smit, T. Tyliszczak, J. Raabe, A. P. Hitchcock, M. Obst, F. M. F. de Groot, and A. V. Petukhov, Langmuir **28**, 3614 (2012).

[26] P. Pieranski, L. Strzelecki, and B. Pansu, Phys. Rev. Lett. **50**, 900 (1983).

[27] S. Neser, C. Bechinger, P. Leiderer, and T. Palberg, Phys. Rev. Lett. **79**, 2348 (1997).

[28] N. Denkov, O. Velev, P. Kralchevski, I. Ivanov, H. Yoshimura, and K. Nagayama, Langmuir **8**, 3183 (1992).

[29] R. Bubeck, S. Neser, C. Bechinger, and P. Leiderer, in *Trends in Colloid and Interface Science XII*, edited by G. Koper, D. Bedeux, W Sager, and C. Cavaco, Progress in Colloid and Polymer Science Vol. 110 (Springer, Berlin/Heidelberg, 1998).

[30] M. Abkarian, J. Nunes, and H. A. Stone, J. Am. Chem. Soc. **126**, 5978 (2004).

[31] H. Bodiguel, F. Doumenc, and B. Guerrier, Langmuir **26**, 10758 (2010).

[32] N. A. M. Verhaegh, J. S. Vanduijneveldt, A. Vanblaaderen, and H. N. W. Lekkerkerker, J. Chem. Phys. **102**, 1416 (1995).

[33] A. V. Petukhov, D. G. A. L. Aarts, I. P. Dolbnya, E. H. A. de Hoog, K. Kassapidou, G. J. Vroege, W. Bras, and H. N. W. Lekkerkerker, Phys. Rev. Lett. **88**, 208301 (2002).

[34] M. E. R. Shanahan, and K. Sefiane, in *Contact Angle, Wettablity and Adhesion*, edited by K. L. Mital (Brill Academic Publishers, Leiden, 2009), Vol. 6, pp. 19–32.

[35] K. Kondiparty, A. Nikolov, S. Wu, and D. Wasan, Langmuir **27**, 3324 (2011).

[36] H. Hu and R. G. Larson, J. Phys. Chem. B **106**, 1334 (2002).

[37] K. Sefiane, S. K. Wilson, S. David, G. J. Dunn, and B. R. Duffy, Phys. Fluids **21**, 062101 (2009).

[38] S. Das, S. Chakraborty, and S. K. Mitra, Phys. Rev. E **85**, 046311 (2012).

[39] L. L. Meng, H. Wei, A. Nagel, B. J. Wiley, L. E. Scriven, and D. J. Norris, Nano Lett. **6**, 2249 (2006).

[40] H. J. Schöpe, A. B. Fontecha, H. Konig, J. Marques-Hueso, and R. Biehl, Langmuir **22**, 1828 (2006).

[41] D. D. Brewer, J. Allen, M. R. Miller, J. M. de Santos, S. Kumar, D. J. Norris, M. Tsapatsis, and L. E. Scriven, Langmuir **24**, 13683 (2008).